LEVERAGING SENSORS FUSION TO ENHANCE ONE-WAY LUNAR NAVIGATION SIGNALS

Michele Ceresoli(1), **Giovanni Zanotti**(2), **Michèle Lavagna**(3)

(1)*Politecnico di Milano, Italy, michele.ceresoli@polimi.it*
(2)*Politecnico di Milano, Italy, giovanni.zanotti@polimi.it*
(3)*Politecnico di Milano, Italy, michelle.lavagna@polimi.it*

ABSTRACT

In the recent years, the Moon has been identified as a key testing ground to develop and enhance technologies for future deep-space missions. For this reason, the European Space Agency (ESA) has launched the Moonlight initiative to foster the development of a dedicated Lunar Communication and Navigation System (LCNS) that offers a one-way navigation service exploiting a small satellite constellation in lunar orbits. However, at the beginning of the constellation setup, a key challenge will be the limited availability of navigation signals, due to the significantly smaller number of LCNS servicing satellites with respect to well-established Earth Global Navigation Satellite Systems (GNSS). To overcome these limitations, the present paper investigates strategies to mitigate the impact of the LCNS blind windows on the estimation process. A tightly coupled navigation architecture is proposed to integrate the LCNS signals with measurements from Inertial Measurement Units (IMUs), altimeters and two-way-ranging with the Lunar Gateway (LOP-G). The observability gains provided by each sensor are here analyzed as a function of the relative servicer-user dynamics and the expected achievable navigation performance are reported for users on polar and equatorial low lunar orbits.

1 INTRODUCTION

The exploration of the Moon has been recognized by the International Space Exploration Coordination Group (ISECG) as a crucial milestone for developing and perfecting key technologies necessary for sustained human presence and exploration in deep-space. Consequently, there has been a global resurgence in lunar missions, attracting participation from both space agencies and private actors. Although these missions have different objectives, they all require precise knowledge of the spacecraft's position and trajectory, as well as a robust communication infrastructure to facilitate the transmission of large volumes of data back to Earth.

Until now, Direct-to-Earth (DTE) communications and ranging radiometric measurements from ground have served as the backbone of lunar missions. However, as the number of potential users continues to grow, several space agencies have proposed the realisation of dedicated lunar communication and navigation infrastructures to relax the Earth ground-segment service demands and provide more efficient and reliable communication links [1] [2]. In this regard, ESA has launched the Moonlight initiative, aiming to provide a cost-efficient and high-performance dedicated Lunar Communication and Navigation Service (LCNS) to support the next generation of institutional and commercial lunar missions. The LCNS infrastructure will allow a constant contact with Earth, even in case of DTE link unavailability (e.g., on the Moon far side) as well as high precision navigation products. Additionally, LCNS could facilitate the on-board implementation of autonomous lunar navigation systems enabling rovers, landers and spacecraft to explore the lunar environment whilst meeting the strict requirements identified by the ISECG to safely operate on the Lunar surface, such as landing within a 90 meters 3-sigma uncertainty from the targeted location.

The LCNS system will provide a one-way service similar to that of Earth Global Navigation Satellite System (GNSS), where each user is able to estimate its position and velocity using standard Time-of-Arrival (ToA) approaches. The broadcasted radio navigation signal will then include the estimated ephemerides of the servicing satellites orbits and the clocks synchronisation errors. One of the major advantages of such system is the great heritage coming from Earth GNSS experience, which allows for a large reuse of the existing technologies. Additionally, it could foster the development of smaller platforms, because of both the lower costs and reduced Size, Weight and Power (SWaP) demands of the required navigation equipment.

At the beginning of the constellation setup, a key challenge will be the limited availability of navigation signals, due to the significantly smaller number of LCNS servicing satellites with respect to the well-established Earth GNSS. In particular, the initial architecture will focus on maximising the navigation performance of surface and Low Lunar Orbital (LLO) users at latitudes around the South Pole region, which is the subject of great scientific interest. Nevertheless, even for South Pole users, the LCNS constellation will still be too small to provide a continuous view of at least 4 satellites at any location, requiring the development of tailored navigation algorithms to cope with the mission requirements.

For these reasons, in the last years several researches have started investigating the achievable performance levels for various lunar missions exploiting potential LCNS-like constellations. In particular, a sequential Extended Kalman filter (EKF) was exploited in [3] to highlight the advantages in terms of system complexity of implementing an LCNS infrastructure over traditional visual-based navigation sensors and ground-tracking techniques, showing that a formal horizontal dilution of precision below 30m can be achieved with a minimum of 3 satellites in visibility. A Batch filter was instead employed by [4] to merge the LCNS signals with IMU and altimeter readings, leading to navigation errors below 30m. In both cases, the estimation is based on a kinematic approach, meaning that during signal outages the navigation error would quickly diverge. The benefits of a dynamic estimation process have been discussed in [5] and [6]. The resulting performance is strongly dependent on the precision of the on-board dynamical model: accurate models require knowledge of the Sun and Earth ephemerides, together with the harmonic coefficients for the spherical expansion of the irregular lunar gravity field. However, not all of these demands may be compatible with low-cost hardware and Commercial-Off-The-Shelf (COTS) components, in particular when the filter must be run at high frequencies.

With this in mind, the goal of the current paper is to further expand our previous work in [5], investigating strategies to mitigate the impact of the reduced-LCNS-visibility windows on the estimation process by integrating one-way ranging with Inertial Measurement Units (IMUs), altimeters and Two-Way-Ranging (TWR) measurements. In particular, the observability gain provided by each sensor will be discussed as function of the relative servicer-user dynamics. Finally, the performance of several explicit Runge-Kutta integration schemes and dynamic approximations will be tested in order to perform a trade-off between solution accuracy and computation burden of the algorithm.

The contents of this paper are organised as follows. In Section 2.1, the scenario and simulation settings are analysed. Section 2.3 provides a detailed mathematical description of the adopted sensor models, whereas the proposed navigation algorithm is discussed in Section 2.4. Section 3 illustrates the navigation performance simulation results and finally, the conclusions are drawn in Section 4.

2 BACKGROUND

2.1 Baseline Mission Scenario

This article will consider lunar users located on polar and equatorial circular Low Lunar Orbits (LLO) at an altitude of 10 km. This kind of orbits are foreseen to be of great importance in future Moon exploration missions: their close proximity to the lunar surface enables and facilitates scientific operations, such as gravity field detection and reconstruction [7], and lunar reconnaissance missions [8]. Additionally, they are also exploited as loitering orbits for landing missions to allow a precise ground-based orbit reconstruction before the final descent phase towards the lunar surface is started.

To accurately simulate the ground-truth dynamics of LLO users and LCNS servicers, the major gravitational and non-gravitational forces have been modelled. The former include the gravitational attraction of the Moon, the Earth and the Sun. The remaining solar system bodies are not included because their gravitational influence ($1\mathrm{e}^{-12}\ \mathrm{m\,s^{-2}}$ for Jupiter) is negligible over the short-term. The irregularities of the lunar gravity field are considered by modelling the lunar gravitational potential $\mathcal{U}$ in a body-fixed reference frame with a Spherical Harmonic Expansion (SHE) [9], as in Eq. 1:

$$\mathcal{U} = \frac{\mu}{r} + \frac{\mu}{r}\sum_{n=2}^{N}\sum_{m=0}^{n}\left(\frac{R_0}{r}\right)^n \left[\overline{C}_{nm}\cos(m\lambda) + \overline{S}_{nm}\sin(m\lambda)\right]\overline{\mathcal{P}}_{nm}(\sin\phi) \tag{1}$$

where μ and R_0 are the gravitational parameter and radius of the Moon, r is the radial distance from the center of mass, λ is the east longitude, ϕ is the latitude and $\overline{\mathcal{P}}_{nm}$ are the fully normalised associated Legendre polynomials. The normalised gravity coefficients ($\overline{C}_{nm}$ and $\overline{S}_{nm}$) are based on the GL0660B gravity model from the GRAIL mission [7]. The potential resulting from Eq. 1 is expressed in the lunar Principal Axes (PA) body-fixed frame, whose orientation data is available in the JPL planetary ephemerides DE421 [10]. The harmonic expansion is truncated at order and degree 60 and is such that the error introduced by neglecting the higher-order terms at these altitudes is below the sensitivity of traditional on-board accelerometers. The effect of solid lunar tides ($\sim 1\mathrm{e}^{-6}\ \mathrm{m\,s^{-2}}$) is modelled by properly modifying the original $\overline{C}_{nm}$ and $\overline{S}_{nm}$ coefficients. For the Sun and Earth contributions, only the point-mass gravitational acceleration is relevant. In particular, Earth's J_2 term produces an acceleration in the order of only $1\mathrm{e}^{-11}\ \mathrm{m\,s^{-2}}$. All the remaining field forces such as general relativistic effects ($\sim 1\mathrm{e}^{-10}\ \mathrm{m\,s^{-2}}$) can be safely neglected for short-term propagations.

The main non-gravitational perturbations acting on the spacecraft are the Solar Radiation Pressure (SRP), the spacecraft thermal emission, the lunar albedo and thermal infrared emission and the navigation antenna thrust for the LCNS servicers. In this analysis, only the SRP contribution is taken into account since it is by far the largest non-gravitational acceleration. A standard *cannonball* model is used to express the magnitude of the SRP acceleration, as shown in Eq. 2:

$$a_{SRP} = \frac{S_{\odot}}{c}\frac{(1\mathrm{AU})^2}{d_{\odot}^2}c_R\frac{A_{\odot}}{m} \tag{2}$$

where $S_{\odot} = 1367\,\mathrm{W\,m^{-2}}$ is the Sun mean flux at 1AU, $c = 299\,792\,458\,\mathrm{m\,s^{-1}}$ is the speed of light, $d_{\odot}$ is the current Sun-spacecraft distance, c_R is the reflectivity and $A_{\odot}$ is the cross-sectional area of the satellite exposed to the radiation. Although a traditional *box-wing* model provides a more accurate representation of the SRP acceleration [11], this simplified model allows to decouple the user trajectory from the geometry and actual orientation of the spacecraft. The user satellite is assumed to have a mass of $100\,\mathrm{kg}$ and a ballistic coefficient of $25\,\mathrm{kg\,m^{-2}}$.

2.2 LCNS Constellation

The nominal orbits for the Moonlight LCNS constellation are still to be officially defined, therefore the orbital baseline considered throughout this analysis is based on the work performed in our previous studies [5] [12]. A 4-satellite constellation deployed on three different orbital planes, spaced in right ascension is here considered. In particular, the satellites are placed on Elliptical Lunar Frozen Orbits (ELFO), whose stability properties with respect to orbital perturbations allow a reduction of the station-keeping budget [13]. The orbits semi-major axes are set to 9750.7 km to ensure a period of 24 hours and the arguments of pericenter are fixed to $90°$ such that the aposelene lies above the South Pole. These choices guarantee extended coverage over the southern lunar hemisphere and may facilitate ground operations on Earth.

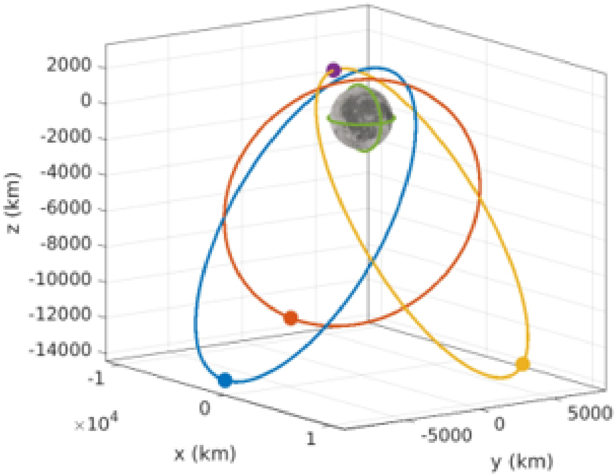

Figure 1: LCNS constellation orbital configuration.

The limited number of servicing satellites with respect to well-established Earth GNSS constellations (e.g., GPS and Galileo) is intended to mimic the initial phase of the Moonlight initiative, which will focus on maximising the navigation performance of surface and LLO users in the neighborhoods of the South Pole region while limiting the overall development and constellation deployment costs.

To simplify the analysis, the availability of the signal from the j-th servicer to a generic user is constrained only by point-to-point and Field-Of-View (FOV) considerations. This aspect will be improved in future studies once the LCNS radio navigation payload and frequencies will be defined. The antenna transmitting the one-way LCNS navigation message on-board the servicing satellites is assumed to be nadir-pointing, while the user antenna is always pointing towards the -Z direction of the ICRF frame. This assumption is intended to maximise the signal availability given that the aposelene of the LCNS servicers is located below the lunar South Pole.

2.3 User Navigation Equipment and Observables

In this work, the adopted LCNS measurements from the generic j^{th} servicer are based on the pseudorange $\tilde{\rho}_j$ and pseudorange-rate $\dot{\tilde{\rho}}_j$. The former is computed with traditional Time-of-Arrival (TOA) techniques, as shown in Eq. 3:

$$\tilde{\rho}_j = \rho_j + c\left(T_u + \delta t_u - T_j - \delta t_j\right) + \varepsilon_{\delta t_j} \tag{3}$$

where ρ_j is the geometric range, c is the speed of light, T_u the system time at which the signal would have reached the user in the absence of errors, δt_u is the receiver clock bias, T_j is the system time at which the signal left the servicer, δt_j is offset of the servicer clock from the system time and $\varepsilon_{\delta t_j}$ is the noise introduced by all the other possible sources of errors, such as interference effects, receiver noise, instrumental delays, multipath losses and relativistic effects. The pseudorange-rate is instead retrieved from Doppler frequency measurements by differencing the nominal carrier frequency and the received signal frequency as in Eq. 4:

$$\tilde{\dot{\rho}}_j = c\frac{\Delta f_D}{f_j} + c\left(\dot{\delta t}_u - \dot{\delta t}_j\right) + \varepsilon_{\dot{\delta t}_j} \tag{4}$$

where $\dot{\delta t}_u$ and $\dot{\delta t}_j$ are the receiver and servicer clock drift errors and $\varepsilon_{\dot{\delta t}_j}$ includes the remaining noises. The formulations of Eqs. 3 and 4 can be further simplified by combining all the error contributions in the single components ε_{ρ_j} and $\varepsilon_{\dot{\rho}_j}$ as per Eqs. 5 and 6:

$$\tilde{\rho}_j = \rho_j + b_c + \varepsilon_{\rho_j} \tag{5}$$

$$\tilde{\dot{\rho}}_j = \dot{\rho}_j + d_c + \varepsilon_{\dot{\rho}_j} \tag{6}$$

where $\dot{\rho}_j$ is the true range-rate, while b_c and d_c are the receiver clock bias and drift in meters and meters per second. These two terms are modelled using the two-state clock model presented in [14], in which the frequency deviation (i.e., the clock drift) is originated from two types of noise, a White Frequency Modulation (WFM) and a Random Walk Frequency Modulation (RWFM). The resulting clock bias will then be represented by a Wiener noise plus an integrated Wiener noise. The dynamical system that simulates the evolution of these quantities is summarised in Eq. 7, in which ε_b and ε_d are Gaussian white noises, whose standard deviation can be properly tuned to match the Allan variance of the desired type of receiver clock.

$$\begin{bmatrix} \dot{b}_c \\ \dot{d}_c \end{bmatrix} = \begin{bmatrix} 0 & 1 \\ 0 & 0 \end{bmatrix} \begin{bmatrix} b_c \\ d_c \end{bmatrix} + \begin{bmatrix} \varepsilon_b \\ \varepsilon_d \end{bmatrix} \tag{7}$$

Inside the navigation filter, the pseudorange and pseudorange-rate will be predicted exploiting the information broadcast within the navigation message to compute the position and velocity of the LCNS satellites and the corrections to synchronise the servicers clocks to system time. For Galileo and GPS, the broadcast ephemerides are the in form of 16 quasi-Keplerian parameters that allow to compute the state of the GNSS satellites in the Earth-Centred Earth-Fixed (ECEF) frame [15]. At the current stage of Moonlight, the structure and the update frequency of the broadcast navigation message is yet to be defined, therefore the residual errors of the predictions coming from the Orbit Determination and Time Synchronisation (ODTS) process performed on ground, also known as Signal In Space Error (SISE) are modelled as simple additive Gaussian white noises, as shown in Eq. 8:

$$\tilde{\mathbf{x}}_j = \left[\tilde{\mathbf{r}}_j^T,\ \tilde{\mathbf{v}}_j^T\right]^T = \mathbf{x}_j + \left[\varepsilon_r^{1\times 3},\ \varepsilon_v^{1\times 3}\right]^T \tag{8}$$

where $\tilde{\mathbf{x}}_j$ are the estimated LCNS ephemerides, while ε_r and ε_v are the SISE position and velocity errors. It is further assumed that the retrieved states of the LCNS satellites are expressed in the ICRF frame, as a proper definition of an official Moon-Centred Moon-Fixed (MCMF) frame is still not available.

During the initial phases of Moonlight, LCNS receivers will be coupled with other traditional sensors, such as Inertial Measurement Units (IMU), laser altimeters and optical cameras to provide a robust estimate of the user trajectory and cope with the limited signal availability. Within this study, we will considers different combinations of the aforementioned sensors to investigate the observability enhancements as function of the user trajectory.

An accelerometer provides a measure of the non-gravitational acceleration of the spacecraft. In this case, given the dynamical environment illustrated in Section 2.1, the sensor would output the acceleration induced by the SRP. A high-fidelity model for an accelerometer typically includes misalignment and cross-axis sensitivity errors, sensor biases and scale factor errors. For the purpose of this work, the model has been simplified and all the errors have been collected into an additive Gaussian white noise, with a standard deviation that is representative of commercial high-fidelity accelerometers.

When combined with LCNS measurements, altimeters can provide a direct estimate of the vertical position in a user-centred East-North-Up (ENU) reference frame. In the current work, the simulated altimeter readings are synthetically generated by perturbing the vertical component of the spacecraft with an additive Gaussian white noise. To simulate the performance of current laser altimeter technology, the standard deviation is set proportional to the 1% of the real user height [16] [17].

The final observables that will be investigated within this study are obtained from Two-Way Ranging (TWR) with the Lunar Orbital Platform-Gateway (LOP-G), a future space station which will be located on a 9:2 resonant Near Rectilinear Halo Orbit (NRHO) around the Moon. In this technique, differently from one-way ranging, the measured pseudorange and pseudorange-rate between the two spacecraft hold irrespective of the receiver clock offset, and effectively provide a more reliable measure with respect to the standard OWR observables. From a practical viewpoint, it is assumed that a deep-space transponder can be mounted on the user spacecraft to allow establishing a link even when the LOP-G is at the aposelene of the NRHO, about 70.000 km away from the Moon. Indeed, this type of transponder has recently been successfully tested over distances up to 6.46 million km [18]. Finally, given that the LOP-G will be a manned spacecraft, we assume that accurate ephemerides from ground observations will be available for uploading to allow the computation of the predicted TWR pseudorange and pseudorange-rate quantities.

2.4 Navigation Algorithm

In present day technology, the different integration techniques to merge GNSS signals with Inertial Navigation System (INS) estimates and the information provided by other sensors can be grouped in three categories:

- *Loose Integration*: in a loosely coupled approach, a self-contained module leverages the incoming GNSS signals to provide a Position, Velocity and Timing (PVT) solution using either Single Point Positioning (SPP) or Precise Point Positioning (PPP) algorithms [19]. This navigation solution is later exploited, together with the other observables, to reduce the drift of the simplified on-board dynamical model during the update step. This option leads to simpler navigation architectures and does not require much knowledge of the GNSS service (e.g., ephemeris computations and clock models). However, its major downside is that PVT estimates can be computed only when signals from at least 4 GNSS satellites are available.

- *Tight Integration*: in a tightly coupled architecture, the GNSS module tracks the incoming radio signals to determine the pseudorange and Doppler measurements, along with the GNSS satellites ephemeris data. This information is then directly used in the filter measurement equations to update the state estimate. Although this approach requires a more complicated design, it holds irrespective of the number of visible GNSS satellites because it is able to utilize the limited number of signals to partially mitigate the navigation error.

- *Deep Integration*: in a deeply coupled system, the filter and the GNSS receiver are combined at the signal processing level. In particular, the filter pseudorange and Doppler predictions are injected into the GNSS receiver carrier-phase and code tracking algorithms to aid the processing of the incoming signals [20]. This integration scheme further enhances the tight coupling advantages by allowing for faster and weaker GNSS signal acquisition, however it requires direct access to the receiver software and alterations of the signal tracking loops.

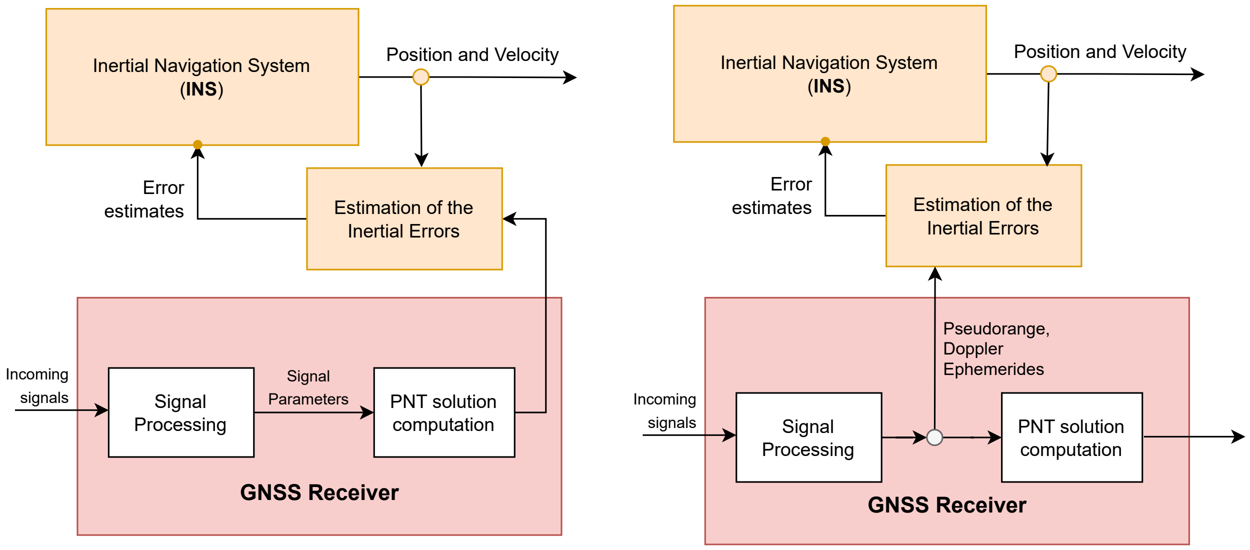

Figure 2: Comparison between loosely-coupled (left) and tightly-coupled (right) architectures

A loose integration is the preferred option to exploit GNSS signals in Low Earth Orbit (LEO) navigation algorithms since many signals from the well-established GNSS constellations are available. However, in the proposed scenario, the limited number of LCNS satellites implies that a loosely-coupled approach would rarely be able to provide a PVT estimate during the initial phases of Moonlight. Additionally, for some orbital inclinations (e.g., equatorial LLOs, see Fig. 4), the user never receives 4 different LCNS signals, meaning it would have to solely rely on the remaining sensors and the on-board propagation to estimate the user position. On the other hand, a deep integration was discarded because code tracking algorithms have not been investigated in the present study. Therefore a tightly coupled integration scheme has been selected to integrate the LCNS observables with the remaining sensors.

The navigation algorithm is based on an Extended Kalman Filter (EKF) that estimates the user inertial position $\hat{\mathbf{r}}$ and velocity $\hat{\mathbf{v}}$ together with the receiver clock bias $\hat{b}_c$ and drift $\hat{d}_c$. The overall state vector is expressed as: $\hat{\mathbf{x}} = [\hat{\mathbf{r}}^\top, \hat{\mathbf{v}}^\top,\ \hat{b}_c,\ \hat{d}_c]^\top$. A dedicated orbital dynamical model is used to accurately estimate the orbital states and cope with the limited observables availability. In practice, a trade-off between model accuracy and computational cost has been performed to account for the reduced computational power of the on-board hardware. In particular, the modelled gravitational accelerations include Moon's central gravity and J_2 contribution together with Earth's third-body perturbation. It is here assumed that dedicated look-up tables or Chebyshev's polynomials coefficients can be stored on-board and/or periodically updated to allow the computation of Earth's position at the current epoch. On the other hand, IMU measurements are exploited to account for the action of non-gravitational accelerations (i.e., the SRP). The complete state prediction equation $\mathbf{f}$ is summarised in Eq. 9:

$$\mathbf{f}(\hat{\mathbf{x}},\ \tilde{\mathbf{a}}_{IMU}) = \begin{cases} \dot{\hat{\mathbf{r}}} = \hat{\mathbf{v}} \\ \dot{\hat{\mathbf{v}}} = \mathbf{a}_M(\hat{\mathbf{r}}) + \mathbf{a}_E(\hat{\mathbf{r}}) + \mathbf{a}_{J_2}(\hat{\mathbf{r}}) + \tilde{\mathbf{a}}_{IMU} \\ \dot{\hat{b}}_c = \hat{d}_c \\ \dot{\hat{d}}_c = 0 \end{cases} \tag{9}$$

The position and velocity components in Eq. 9 are discretely integrated using an explicit Runge-Kutta (RK) integration scheme. A trade-off between integration order and computational demands (i.e., number of evaluations of $\mathbf{f}$) is reported in Table 1 to identify the most suitable RK method for efficient on-board implementations. On the other hand, the clock states are integrated with a simple Euler model. The associated a-priori state covariance matrix is computed as in Eq. 10:

$$\mathbf{P}_k^- = \mathbf{F}_{k-1}\mathbf{P}_{k-1}^+\mathbf{F}_{k-1}^T + \mathbf{\Gamma}_{k-1}\mathbf{Q}_{k-1}\mathbf{\Gamma}_{k-1}^T \tag{10}$$

where $\mathbf{F}_{k-1}$ is the State Transition Matrix (STM), evaluated from the Jacobian of Eq. 9 using a 2^{nd} order approximation. The process noise transition matrix $\mathbf{\Gamma}_{k-1}$ is instead computed assuming that the effect of the unmodelled accelerations and disturbances over the interval $[t_{k-1},\ t_k]$ can be approximated by an impulsive action exerted at t_{k-1}, which is a reasonable assumption for small integration times.

The measurement equations implemented in the correction step to predict the LCNS observables (i.e., the pseudorange and Doppler) are reported in Eqs. 11 and 12:

$$\hat{\rho}_j = \|\tilde{\mathbf{r}}_j - \hat{\mathbf{r}}\| + \hat{b}_c \tag{11}$$

$$\hat{\dot{\rho}}_j = (\tilde{\mathbf{v}}_j - \hat{\mathbf{v}}) \cdot (\tilde{\mathbf{r}}_j - \hat{\mathbf{r}})/\hat{\rho} + \hat{d}_c \tag{12}$$

where the LCNS satellites ephemerides measurements $\tilde{\mathbf{r}}_j$ and $\tilde{\mathbf{v}}_j$ are generated according to Eq. 8. The LOP-G TWR pseudorange and Doppler predictions are very similar to Eqs. 11 and 12 but do not account for the clock bias and drift. On the other hand, the altimeter readings are predicted using Eq. 13:

$$h = \|\hat{\mathbf{r}}\| - R_M \tag{13}$$

where R_M is the reference radius of the Moon. Finally, the a-posteriori state $\hat{\mathbf{x}}_k^+$ and covariance matrix $\mathbf{P}_k^+$ are computed similarly to traditional EKF implementations, as shown in Eqs. 14-17:

$$\mathbf{z}_k = \tilde{\mathbf{y}}_k - \mathbf{h}(\hat{\mathbf{x}}_k^-) \tag{14}$$

$$\mathbf{K}_k = \mathbf{P}_k^-\mathbf{H}_k^T(\mathbf{H}_k\mathbf{P}_k^-\mathbf{H}_k^T + \mathbf{R}_k)^{-1} \tag{15}$$

$$\hat{\mathbf{x}}_k^+ = \hat{\mathbf{x}}_k^- + \mathbf{K}_k\mathbf{z}_k \tag{16}$$

$$\mathbf{P}_k^+ = (\mathbf{I} - \mathbf{K}_k\mathbf{H}_k)\mathbf{P}_k^-(\mathbf{I} - \mathbf{K}_k\mathbf{H}_k)^T + \mathbf{K}_k\mathbf{R}_k\mathbf{K}_k^T \tag{17}$$

where $\tilde{\mathbf{y}}_k$ are the available measurements at step k, $\mathbf{h}$ and $\mathbf{H}_k$ are the measurement prediction equations and their Jacobian (evaluated at $\hat{\mathbf{x}}_k^-$), $\mathbf{R}_k$ is the measurement covariance matrix and $\mathbf{K}_k$ the Kalman gain. Eq. 17 exploits the Joseph covariance correction formulation to ensure that $\mathbf{P}_k$ remains positive definite.

3 RESULTS

3.1 Dynamical Prediction Models

To select the most suited RK integration scheme for the prediction step of the EKF, a sensitivity analysis has been performed and the results are shown in Table 1. For this analysis, the user was settled on a polar LLO at 10 km from the Moon surface. Additionally, to maximise the blind windows durations (i.e., the time intervals where the filter must rely on its own on-board propagation model because no LCNS signal is available) only the LCNS observables were considered. The reported time benchmarks have been obtained with a Julia implementation on an Intel Core i7-6700 CPU @ 3.40 GHz.

Table 1: Sensitivity analysis for different Runge-Kutta integration methods at 1 Hz.

Method	No. Stages	Time (μs)	RMSE$_{pos}$ (m)	RMSE$_{vel}$ (m/s)
Euler	1	3.601	1467.4	1.492
Heun	2	4.147	506.5	0.445
Tsitouras 5(4)	6	5.743	503.4	0.436
Verner 7(6)	10	7.722	503.1	0.434

The Root Mean Square Errors (RMSE) clearly show that even at 1 Hz, the Euler scheme leads to unacceptable navigation errors. On the other hand, the differences between the Heun and the remaining integration schemes are in the order of few meters. This result highlights that an EKF running at 1 Hz can leverage a simple 2-stages Heun method to halve the propagation times with negligible accuracy drops in the estimated solution. For this reason, Heun's scheme has been selected as the baseline RK method for the prediction step of the remaining analyses reported in this paper.

3.2 Navigation Performance

The simulation used to investigate the performance of the proposed navigation architecture includes potential users on polar and equatorial LLO at an altitude of 10 km, whose dynamics has already been illustrated in Section 2.1. These scenarios are meant to be representative of possible parking orbits before the user is injected in the final landing trajectory. A Montecarlo simulation with 200 runs was performed for each combination of user and available sensors. A summary of the adopted simulation parameters and sensor settings is reported in Table. 2.

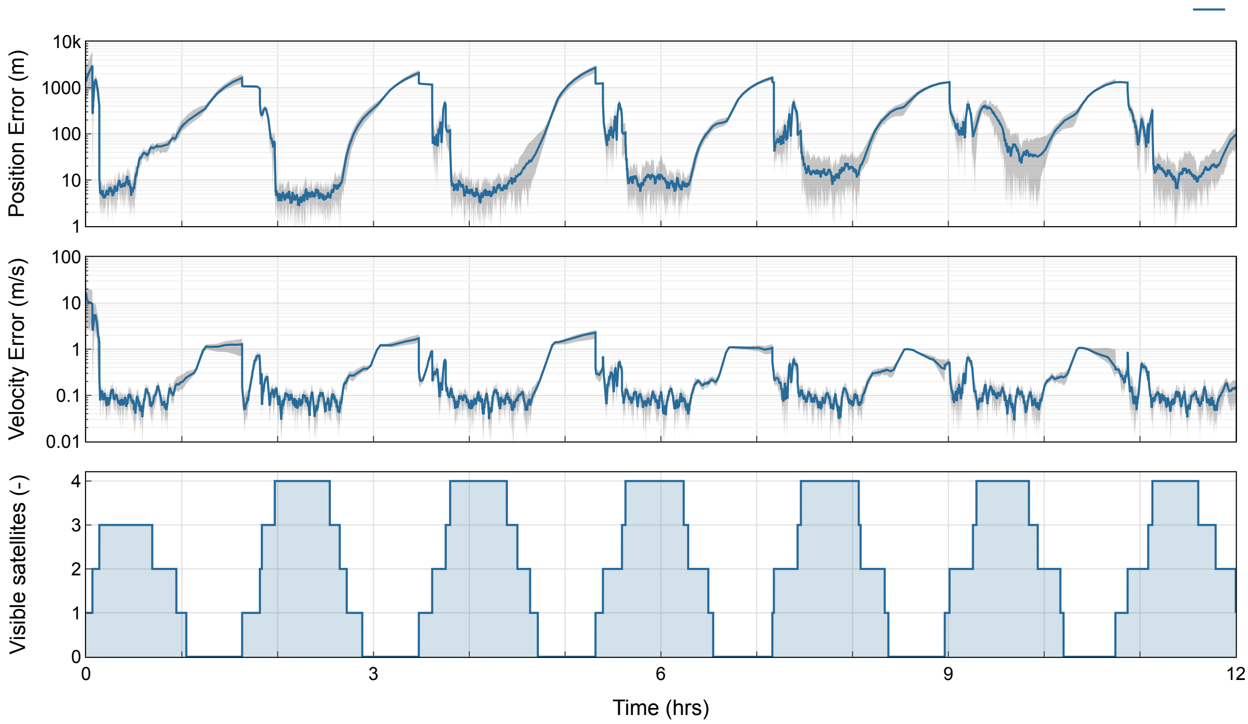

Figure 3: Polar LLO navigation performance with LCNS-only observables. The gray bands represent the 3σ envelope of the Montecarlo simulations.

Table 2: Summary of the navigation simulation parameters.

Parameter	Value
LCNS SISE (1σ)	Position ε_r (x, y, z): 15 m Velocity ε_v (x, y, z): 0.15 m/s Clock bias ε_ρ: 10 m Clock drift $\varepsilon_{\dot{\rho}}$: 0.1 m/s
LCNS measurement rate	1 Hz
LCNS Antenna H-FoV	21°
User clock Allan variance	h_0: 2×10^{-25} h_{-2}: 6×10^{-25}
Altimeter noise (1σ)	100 m
Altimeter measurement rate	1 Hz
IMU noise (1σ)	1 μg
IMU measurement rate	1 Hz
TWR SISE (1σ)	Position ε_r (x, y, z): 10 m Velocity ε_v (x, y, z): 0.1 m/s
TWR measurement rate	0.1 Hz
Initial filter uncertainty (1σ)	Position σ_r (x, y, z): 1 km Velocity σ_v (x, y, z): 100 m/s Clock bias σ_{b_c}: 100 m Clock drift σ_{d_c}: 1 m/s
Filter rate	1 Hz

Figure 3 illustrates the results of the polar user when the filter only receives the LCNS signals. The resulting satellite visibility consists of an alternating pattern between full availability when the user is above the lunar South Pole and blind windows (i.e., signal outages) in proximity of the North Pole, where the LCNS signals are obstructed by the Moon. This pattern slowly shifts throughout the day as the LCNS satellites move towards the periselene of their 24-hours-period orbits. Therefore, each day, there will also be a very short time during which the LLO users will be able to receive LCNS signals above the North Pole instead of the South Pole. The overall duration of the availability windows improves for increasing orbital altitudes. Indeed, higher orbits spend a greater time above the southern hemisphere and LCNS signals are less occultated because of the smaller apparent Moon size.

In terms of navigation accuracy, the optimal constellation geometry leads to extremely small errors (below $10\,\mathrm{m}$) when all the measurements are available but then quickly diverge to about $2000\,\mathrm{m}$ until a new signal is available. In particular, a significant decrement of the performance becomes visible when less than 3 satellites are visible. This divergence could be further mitigated by improving the simplified on-board dynamical propagation model, such as by including higher order harmonics. The velocity errors are instead bounded between $0.1\,\mathrm{m\,s^{-1}}$ and $1\,\mathrm{m\,s^{-1}}$.

On the other hand, although in the equatorial case shown in Fig. 4 no blind windows are present, the user is unable to simultaneously retrieve signals from all the LCNS servicers because of the unfavoraruble user-servicers relative motion. The outcome is an average position error of about $553\,\mathrm{m}$, with few peaks of $1000\,\mathrm{m}$. A reduction of the error to around $100\,\mathrm{m}$ is only possible when a third satellite becomes visible.

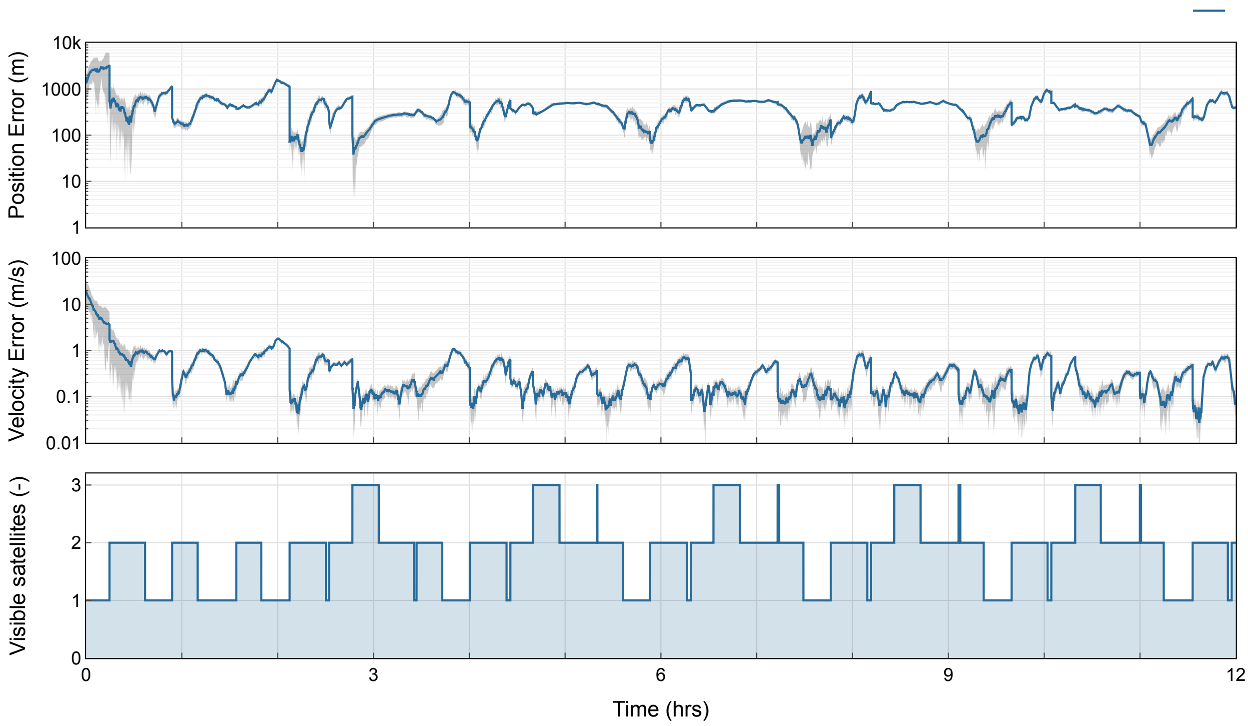

Figure 4: Equatorial LLO navigation performance with LCNS-only observables. The gray bands represent the 3σ envelope of the Montecarlo simulations.

The addition of an altimeter provides a direct estimate of the spacecraft position vertical component, effectively reducing the overall number of unknowns. For the polar LLO user, Fig. 5 shows a comparison between the LCNS-only and the combined LCNS and altimeter observables. In particular, the minimum achievable error is improved to about $4\,\mathrm{m}$. Most importantly, the new additional measurement allows to bound the position error below $10\,\mathrm{m}$ until at least 2 LCNS signals are received. In turn, this reduces the error at the beginning of the blind windows, aiding the on-board propagator and leading to a reduction of almost $1000\,\mathrm{m}$ of the peak position errors. Nevertheless, it is important to highlight that, although the altimeter readings are continuously received, the filter cannot accurately reconstruct the state vector when LCNS signals are unavailable and quickly diverges because the system lacks observability.

The greatest improvement are achieved in the equatorial LLO, as illustrated by Fig. 6. In this case, given that the user almost always has at least 2 LCNS satellites in visibility, the altimeter exploitation reduces the position estimation error below $100\,\mathrm{m}$ for most of the simulation. In practice, these values do not account for the difference between the measured distance and the actual ground, because the Moon is assumed spherical. Accurate DEM models of the lunar surface will need to be exploited to accurately predict the actual height value instead of the one based on a spherical or elliptical approximations. A detailed analysis on this matter will be performed in futures studies.

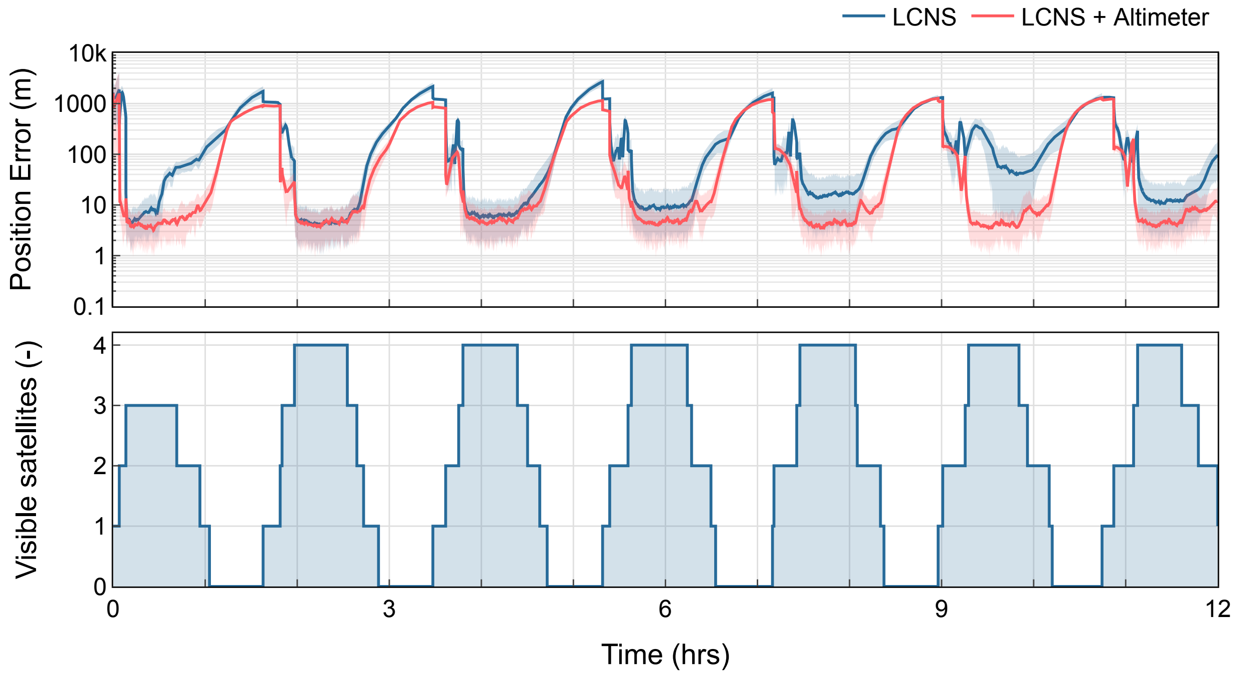

Figure 5: Polar LLO navigation performance comparison between LCNS-only (blue) and combined LCNS-altimeter (red) observables. The blue and red bands represent the 3σ envelopes of the Montecarlo simulations.

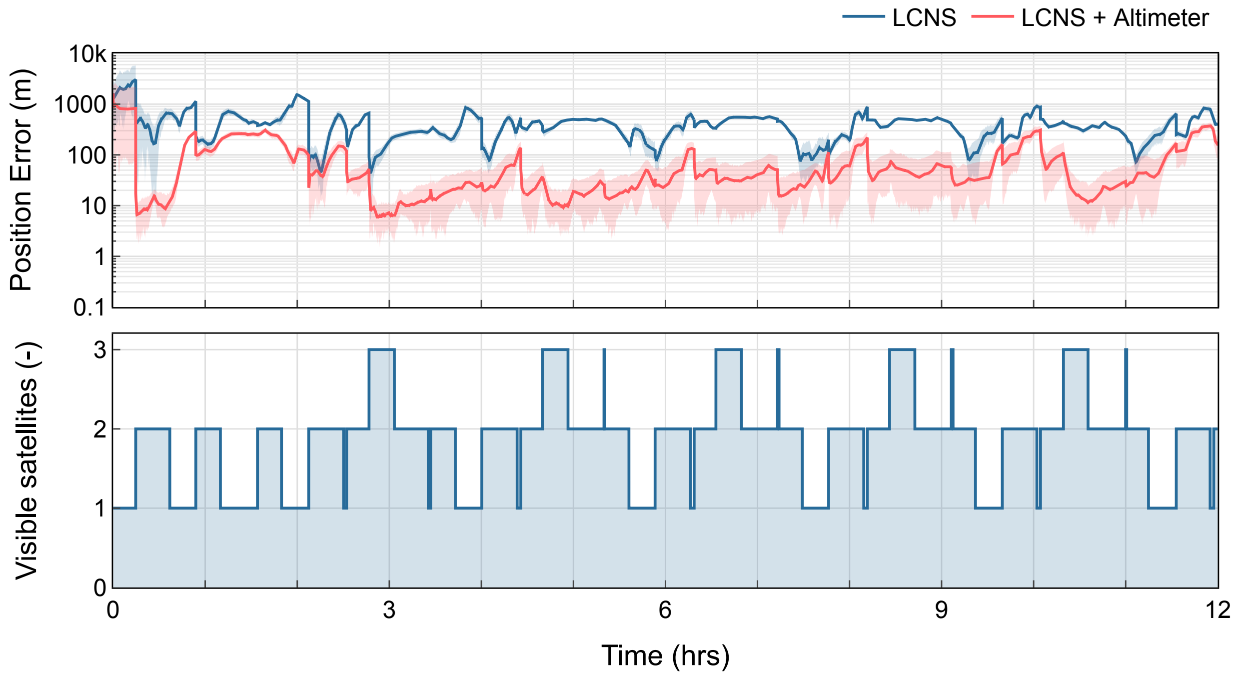

Figure 6: Equatorial LLO navigation performance comparison between LCNS-only (blue) and combined LCNS-altimeter (red) observables. The blue and red bands represent the 3σ envelopes of the Montecarlo simulations.

Finally, the results displayed in Figs. 7 and 8 highlight the navigation performance when also TWR measurements with the LOP-G are exploited. The LOP-G visibility patterns can be explained by recalling that the lunar Gateway will be placed on a southern NRHO, where it will be located for long periods of time below the lunar South Pole.

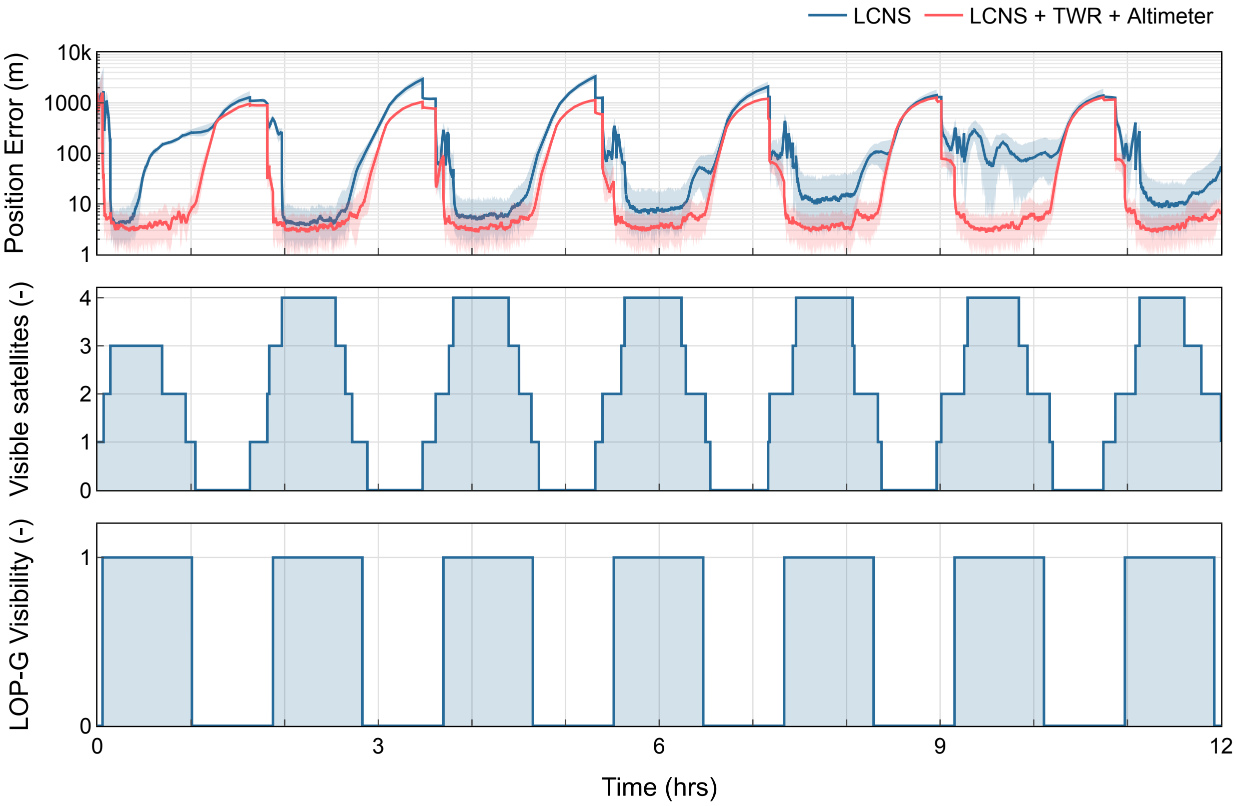

Figure 7: Polar LLO navigation performance comparison between LCNS-only (blue) and the complete sensor suite (red) observables. The blue and red bands represent the 3σ envelopes of the Montecarlo simulations.

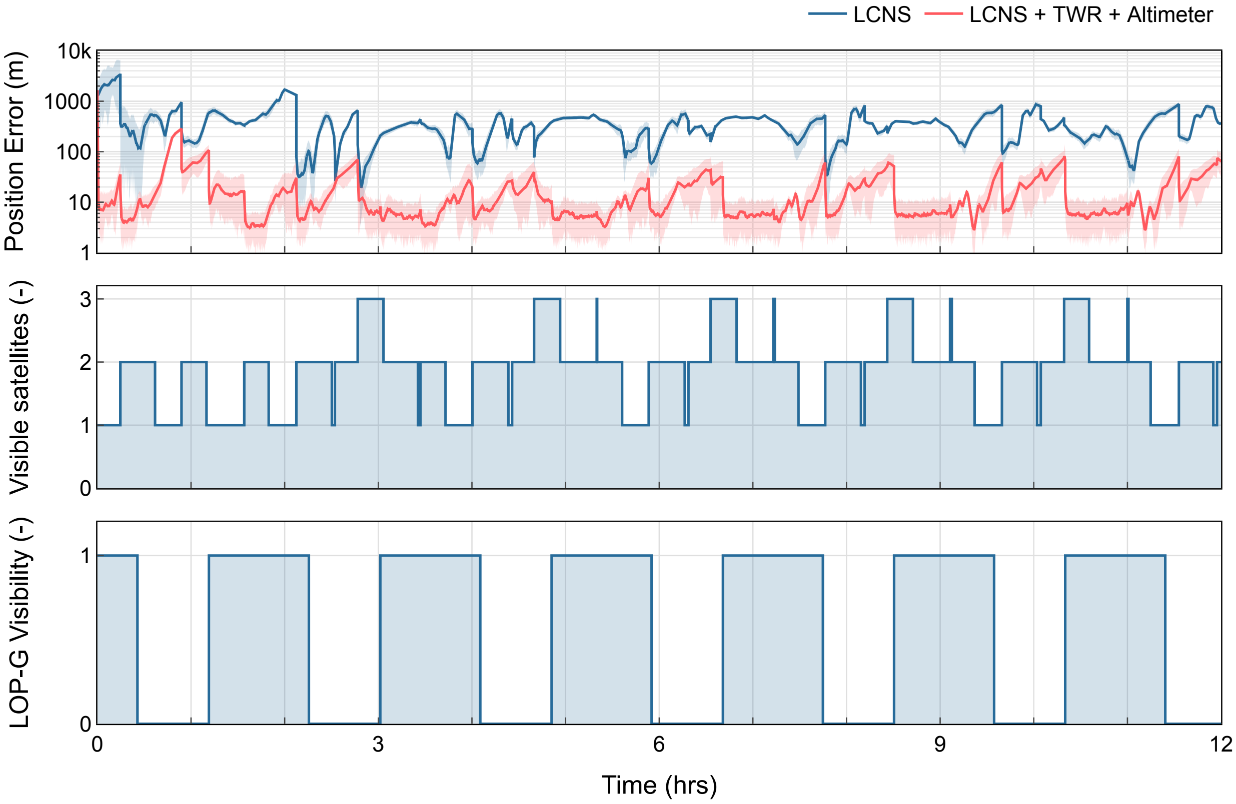

Figure 8: Equatorial LLO navigation performance comparison between LCNS-only (blue) and the complete sensor suite (red) observables. The blue and red represent the 3σ envelopes of the Montecarlo simulations.

For the polar scenario, this additional observable is not as useful as in the equatorial LLO. Indeed, TWR signals are received in proximity of the South Pole, which is already characterised by an optimal LCNS geometry and availability. Additionally, the same signals will be often occulted by the Moon whenever the user is above the northern pole and therefore, are unable to enhance the observability of that critical region. On the other hand, the exploitation of the complete sensor suite introduces a huge advantage for equatorial users. In fact, once the filter has initially converged, the navigation error is almost always below $100\,\mathrm{m}$, with average values of few tens of meters. In this case, the LOP-G visibility still exhibits an alternating pattern due to the combined effects of an extremely low altitude of the LLO orbit and the inclination of the NRHO. Indeed, with the same visibility conditions, when the LOP-G is below the South Pole users at altitude above 100 km are capable of receiving the signals for about 3/4 days without interruptions.

4 CONCLUSIONS

The present study proposed a tightly-coupled navigation architecture to combine one-way ranging signals from a dedicated lunar navigation constellation together with measurements from accelerometers, altimeters and two-way ranging with the lunar Gateway. Two different orbital scenarios, involving both polar and equatorial low lunar orbiters, have been investigated to highlight the observability and performance gain provided by each of the aforementioned sensors. The Montecarlo simulation results highlighted that while a satisfactory navigation accuracy is achievable in the equatorial case with the complete sensor suite, polar LLO users suffer significant performance drops in proximity of the lunar North Pole, where LCNS measurements are often unavailable. In this regard, the divergence can be mitigated either by improving the on-board dynamical model (e.g., by including more orders of the lunar gravitational potential) or by exploiting vision-based navigation algorithms to cope with the limited LCNS availability.

5 ACKNOWLEDGEMENTS

The authors would like to acknowledge Telespazio S.p.A. for providing the funding to support the study presented in this paper under Research Contract No. 20212140.

REFERENCES

[1] D. J. Israel, K. D. Mauldin, C. J. Roberts, *et al.*, “Lunanet: A flexible and extensible lunar exploration communications and navigation infrastructure,” in *2020 IEEE Aerospace Conference*, IEEE, 2020, pp. 1–14.

[2] ESA, *Moonlight: Connecting Earth with the Moon*, 2021. [Online]. Available: `%7Bhttps://www.esa.int/ESA%5C_Multimedia/Videos/2021/05/Moonlight%20%5C_bringing%5C_connectivity%5C_to%5C_the%5C_Moon%7D`.

[3] A. Grenier, P. Giordano, L. Bucci, *et al.*, “Positioning and velocity performance levels for a lunar lander using a dedicated lunar communication and navigation system,” *NAVIGATION: Journal of the Institute of Navigation*, vol. 69, no. 2, 2022.

[4] P. Giordano, A. Grenier, P. Zoccarato, *et al.*, “Moonlight navigation service-how to land on peaks of eternal light,” in *Proceedings of the 72nd International Astronautical Congress (IAC), Dubai, United Arab Emirates*, 2021, pp. 25–29.

[5] G. Zanotti, M. Ceresoli, A. Pasquale, J. Prinetto, and M. Lavagna, “High performance lunar constellation for navigation services to moon orbiting users,” *Advances in Space Research*, 2023.

[6] M. Mangialardo, M. M. Jurado, D. Hagan, P. Giordano, P. Zoccarato, and J. Ventura-Traveset, “Autonomous navigation for moon missions: A realistic performance assessment, considering earth gnss signals and lcns constellation,” in *2022 10th Workshop on Satellite Navigation Technology (NAVITEC)*, IEEE, 2022, pp. 1–11.

[7] A. S. Konopliv, R. S. Park, D.-N. Yuan, *et al.*, “The jpl lunar gravity field to spherical harmonic degree 660 from the grail primary mission,” *Journal of Geophysical Research: Planets*, vol. 118, no. 7, pp. 1415–1434, 2013.

[8] M. Beckman, “Mission design for the lunar reconnaissance orbiter,” in *29th Annual AAS Guidance and Control Conference*, 2007.

[9] D. A. Vallado, *Fundamentals of astrodynamics and applications*. Springer Science & Business Media, 2001, vol. 12.

[10] W. M. Folkner, J. G. Williams, and D. H. Boggs, “The planetary and lunar ephemeris de 421,” *IPN progress report*, vol. 42, no. 178, p. 1, 2009.

[11] G. Bury, K. Sośnica, R. Zajdel, and D. Strugarek, “Toward the 1-cm galileo orbits: Challenges in modeling of perturbing forces,” *Journal of Geodesy*, vol. 94, no. 2, p. 16, 2020.

[12] A. Pasquale, G. Zanotti, J. Prinetto, M. Ceresoli, and M. Lavagna, “Cislunar distributed architectures for communication and navigation services of lunar assets,” *Acta Astronautica*, vol. 199, pp. 345–354, 2022.

[13] T. Nie and P. Gurfil, “Lunar frozen orbits revisited,” *Celestial Mechanics and Dynamical Astronomy*, vol. 130, no. 10, p. 61, 2018.

[14] L. Galleani, “A tutorial on the two-state model of the atomic clock noise,” *Metrologia*, vol. 45, no. 6, S175, 2008.

[15] J. S. Subirana, J. J. Zornoza, and M. Hernández-Pajares, *GNSS Data Processing Vol. I: Fundamentals and Algorithms*. ESA Communications, 2013, vol. 1.

[16] P. Lunghi, M. Lavagna, and R. Armellin, “A semi-analytical guidance algorithm for autonomous landing,” *Advances in Space Research*, vol. 55, no. 11, pp. 2719–2738, 2015.

[17] S. Silvestrini, M. Piccinin, G. Zanotti, A. Brandonisio, P. Lunghi, and M. Lavagna, “Implicit extended kalman filter for optical terrain relative navigation using delayed measurements,” *Aerospace*, vol. 9, no. 9, p. 503, 2022.

[18] H. Noda, H. Senshu, T. Otsubo, *et al.*, “Demonstration of deep-space synchronous two-way laser ranging with a laser transponder aboard hayabusa2,” *Advances in Space Research*, 2023.

[19] P. J. Teunissen and O. Montenbruck, *Springer handbook of global navigation satellite systems*. Springer, 2017, vol. 10.

[20] A. Soloviev, “Gnss-ins integration,” *Position, Navigation, and Timing Technologies in the 21st Century: Integrated Satellite Navigation, Sensor Systems, and Civil Applications, Volume 2*, 2020.